Earth and Planetary Science Letters 418 (2015) 91–102

Contents lists available at ScienceDirect

Earth and Planetary Science Letters

www.elsevier.com/locate/epsl

Tracking the source of the enriched martian meteorites in olivine-hosted melt inclusions of two depleted shergottites, Yamato 980459 and Tissint

T.J. Peters[a,b,c,*], J.I. Simon[b,c], J.H. Jones[b], T. Usui[d], R. Moriwaki[d], R.C. Economos[e], A.K. Schmitt[e], K.D. McKeegan[e]

[a] *Lunar and Planetary Institute, Houston, TX 77058, USA*
[b] *Astromaterials Research and Exploration Science, NASA Johnson Space Center, Houston, TX 77058, USA*
[c] *Center for Isotope Cosmochemistry and Geochronology, NASA Johnson Space Center, Houston, TX 77058, USA*
[d] *Department of Earth & Planetary Sciences, Tokyo Institute of Technology, Tokyo 152-8551, Japan*
[e] *Department of Earth, Planetary, and Space Sciences, University of California, Los Angeles, CA 90095, USA*

ARTICLE INFO

Article history:
Received 11 October 2014
Received in revised form 19 February 2015
Accepted 20 February 2015
Available online 13 March 2015
Editor: T. Mather

Keywords:
martian mantle melting
mantle depletion
olivine-phyric shergottites
olivine-hosted melt inclusions
Rare Earth Elements
crustal recycling

ABSTRACT

The apparent lack of plate tectonics on all terrestrial planets other than Earth has been used to support the notion that for most planets, once a primitive crust forms, the crust and mantle evolve geochemically-independent through time. This view has had a particularly large impact on models for the evolution of Mars and its silicate interior. Recent data indicating a greater potential that there may have been exchange between the martian crust and mantle has led to a search for additional geochemical evidence to support the alternative hypothesis, that some mechanism of crustal recycling may have operated early in the history of Mars.

In order to study the most juvenile melts available to investigate martian mantle source(s) and melting processes, the trace element compositions of olivine-hosted melt inclusions for two incompatible-element-depleted olivine-phyric shergottites, Yamato 980459 (Y98) and Tissint, and the interstitial glass of Y98, have been measured by Secondary Ionization Mass Spectrometry (SIMS). Chondrite-normalized Rare Earth Element (REE) patterns for both Y98 and Tissint melt inclusions, and the Y98 interstitial glass, are characteristically light-REE depleted and parallel those of their host rock. For Y98, a clear flattening and upward inflection of La and Ce, relative to predictions based on middle and heavier REE, provides evidence for involvement of an enriched component early in their magmatic history; either inherited from a metasomatized mantle or crustal source, early on and prior to extensive host crystallization.

Comparing these melt inclusion and interstitial glass analyses to existing melt inclusion and whole-rock data sets for the shergottite meteorite suite, defines mixing relationships between depleted and enriched end members, analogous to mixing relationships between whole rock Sr and Nd isotopic measurements. When considered in light of their petrologic context, the origin of these trace element enriched and isotopically evolved signatures represents either (1) crustal assimilation during the final few km of melt ascent towards the martian surface, or (2) assimilation soon after melt segregation, through melt–rock interaction with a portion of the martian crust recycled back into the mantle.

1. Introduction

Meteorites from Mars provide a unique opportunity to explore the formation and evolution of another planet in the inner-solar system and allow for comparative studies with Earth to help better understand the differentiation and thermal evolution of planetary interiors. The shergottite meteorites are a suite of martian basaltic to lherzolitic igneous rocks that have provided important constraints on the accretion, evolution, structure, and bulk composition of Mars (e.g. McSween and Treiman, 1998). They represent a period of relatively young mantle melting and surface volcanism, ∼ 550–150 Ma (e.g. Nyquist et al., 2001); although crystallization ages of 4.1–4.3 Ga have been proposed (e.g. Bouvier et al., 2008, 2009).

The isotopic and elemental geochemistry of the shergottites span a wide compositional spectrum (Fig. 1); from trace element

---

[*] Corresponding author at: Lunar and Planetary Institute, Houston, TX 77058, USA.
E-mail address: Peterstj2313@gmail.com (T.J. Peters).

http://dx.doi.org/10.1016/j.epsl.2015.02.033

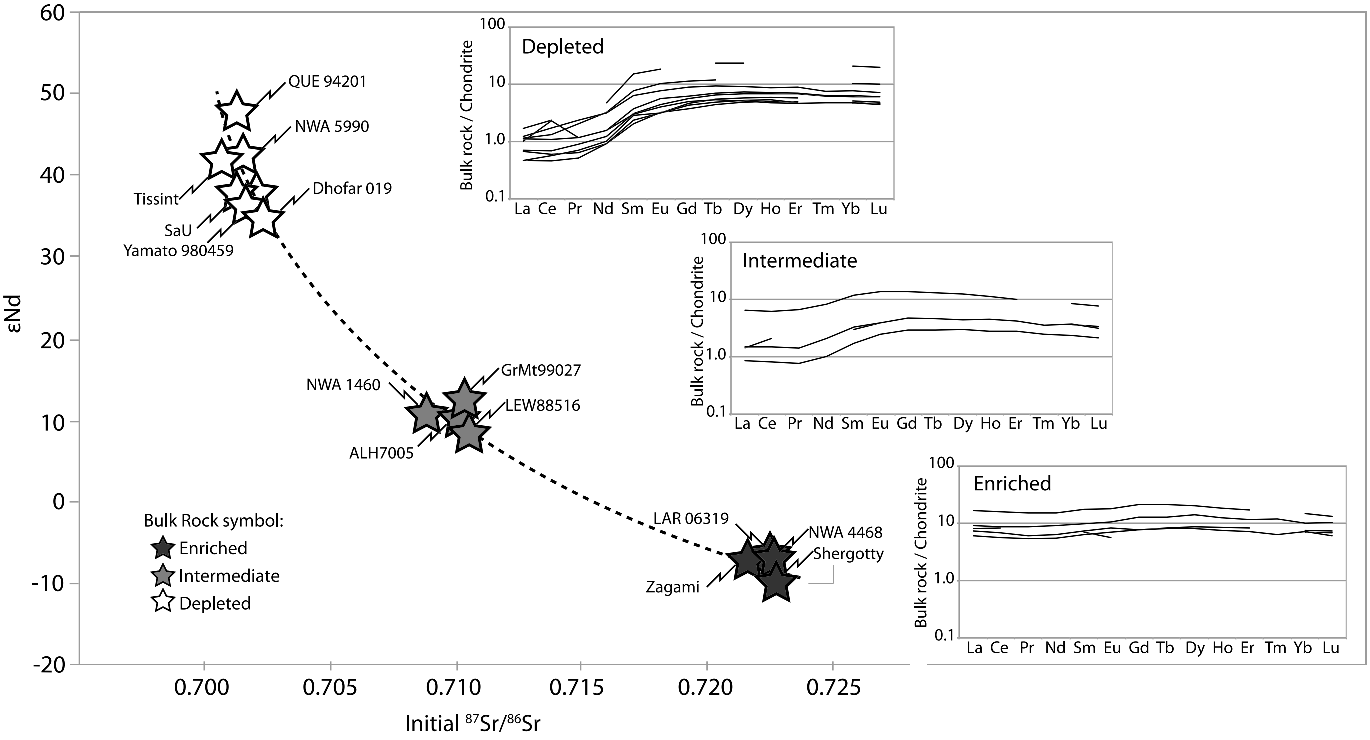

Fig. 1. ε^{143}Nd vs. initial $^{87}Sr/^{86}Sr$ for the shergottite meteorites (after Symes et al., 2008, and references therein). Inserted are whole rock REE patterns that define the three groups; (1) depleted, (2) intermediate, and (3) enriched shergottites. Other isotopic and trace-element data sources are listed in Appendix 6 of the supplementary materials.

depleted and isotopically primitive, to enriched and isotopically evolved. The depleted shergottites are considered partial melts from an initially olivine–pyroxene–garnet cumulate portion of the martian mantle that had undergone extensive melting (e.g. Borg et al., 1997; Borg and Draper, 2003; Shih et al., 2005; Debaille et al., 2008). This history of melting led to significant depletions in elements incompatible, particularly the LREE and radiogenic heat producing elements K, Th, and U (e.g. Borg and Draper, 2003). These trace element depletions are correlated with primitive radiogenic isotope ratios that yield 4.0–4.5 Ga whole-rock model isochron ages, indicative of early mantle depletion during, or immediately following, magma ocean crystallization (e.g. Shih et al., 1982, 2005; Blichert-Toft et al., 1999; Borg et al., 1997; Brandon et al., 2012; Debaille et al., 2008; Bouvier et al., 2005).

The intermediate and enriched shergottites are also considered melts from the depleted mantle, but have experienced variable degrees of contamination from an isotopically evolved and trace element enriched ancient geochemical reservoir (e.g. Borg et al., 1997; Borg and Draper, 2003). This evolved and enriched reservoir is considered to represent either (1) ancient oxidized martian crust, assimilated during emplacement and crystallization of a depleted mantle melt (e.g. Jones, 1989; Usui et al., 2012), or (2) an incompatible-trace-element-rich component, analogous to lunar KREEP, that represents a trapped residual melt formed during fractional crystallization of the martian magma ocean (e.g. Borg et al., 1997; Borg and Draper, 2003; Brandon et al., 2012; Debaille et al., 2008; Symes et al., 2008; Basu Sarbadhikari et al., 2011). Distinguishing between either model and constraining the location of the enriched reservoir relative to the depleted shergottite mantle source, however, remains debated, but has important implications for the geodynamic evolution of the martian mantle, generation of an early martian crust, and the possibly of Earth-like crustal recycling early in the history of Mars.

Here we address the origin(s) of trace element enriched (and isotopically evolved) signatures for the depleted shergottite meteorites using the trace element compositions of olivine-hosted melt inclusions in two depleted olivine-phyric shergottite meteorites, Y980459 (Y98) and Tissint, and the interstitial glass of Y98. The data presented suggests both Y98 and Tissint melt inclusions record the progressive collection of melt components from a residual olivine, orthopyroxene, and garnet mantle source. It is also shown that the origin of an enriched component in Y98 occurs early in its magmatic history, either inherited from its source or incorporated at a time prior to the onset of host crystallization. This early incorporation of enriched trace element signatures is discussed in the context of recent models to represent assimilation of an ancient portion of martian crust, recycled into the upper mantle during an early stage in the history of Mars.

2. Samples

Yamato 980459 (Y98) and Tissint are olivine-phyric shergottite meteorites, displaying a porphyritic texture with olivine megacrysts set among a fine-grained groundmass. They are ∼18 wt% MgO, with <1% total alkalis (i.e. $Na_2O + K_2O$), similar to high-temperature picritic or basaltic komatiitic melts (e.g. Le Bas, 2000), and closely represent true liquids (e.g. Usui et al., 2008; Aoudjehane et al., 2012).

Y98 and Tissint are ideal candidates to probe their primitive mantle source. They are two of the most magnesian shergottites (Y98 Mg#$_{66}$: Shirai and Ebihara, 2004; and Tissint Mg#$_{60}$: Aoudjehane et al., 2012), and have particularly primitive ε^{143}Nd values; +37 at 475 Ma (Fig. 1: Shih et al., 2005) and +44 at 472 Ma (Fig. 1: Shih et al., 2014), for Y98 and Tissint, respectively. These initial ε^{143}Nd values are 4–9 epsilon units lower than that of QUE 94201 (Fig. 1: ε^{143}Nd = 48 at 327 Ma), the best-characterized and most isotopically primitive depleted shergottite (Borg et al., 1997).

Y98 is an Antarctic find and the most mineralogically primitive olivine-phyric shergottite (e.g. Greshake et al., 2004; Usui et al., 2008). The sample studied herein, Y-980459 (51-2), is described in Usui et al. (2008) and contains 12 vol% olivine (6.2 vol% for olivine

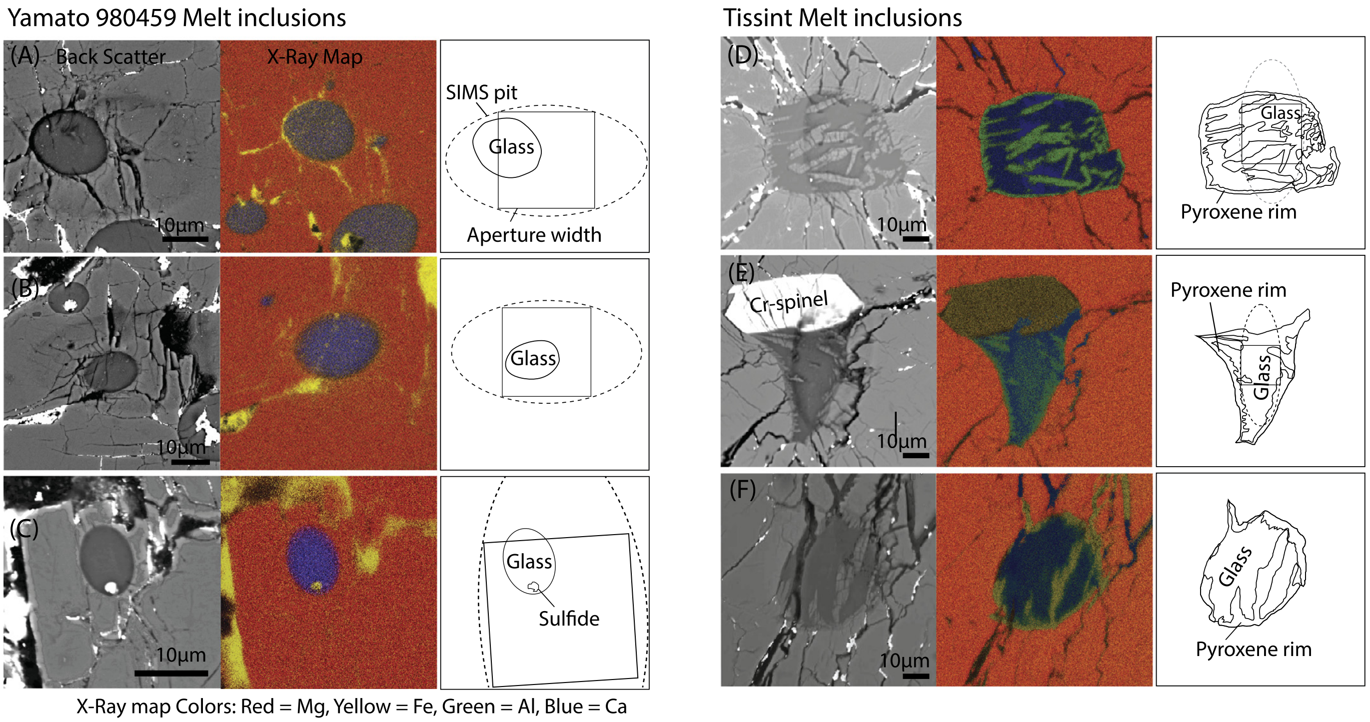

Fig. 2. Backscatter (grey), X-ray (colored), and sketch maps of olivine-hosted melt inclusions in (A–C) Yamato 980459, and (D–F) Tissint analyzed in this study. Note the small size, crystal free Y98 melt inclusions, which contrast markedly with the partially quenched cpx bearing Tissint melt inclusions. Augite dendrites are $En_{28-36}Fs_{14-18}Wo_{50-56}$. X-ray map colors are, Red = Mg, Yellow = Fe, Green = Al, Blue = Ca. (For interpretation of the references to color in this figure legend, the reader is referred to the web version of this article.)

megacrysts with Fo > 80), 58 vol% pyroxene, 23 vol% mesostasis (interstitial glass with abundant olivine and augite dendrites and immiscible sulfide droplets), and 1 vol% spinel. Importantly, Y98 lacks plagioclase/maskelynite or phosphates, which are common groundmass phases for other olivine-phyric shergottites. Experiments have determined a 1 bar liquidus temperature of ∼1450 °C (Koizumi et al., 2004), and that Y98 was quenched before the appearance of plagioclase. As a result, melt inclusions are glassy, similar to the interstitial glass.

Tissint was witnessed to fall over Morocco on 18 July 2011, and consists of olivine megacrysts in a fine-grained groundmass of pyroxene and feldspathic glass (maskelynite), Ti-poor chromite, ilmenite, pyrrhotite and minor merrillite (Aoudjehane et al., 2012). Similar to Y98, Tissint contains 17 vol% olivine (12 vol% for olivine megacrysts) and 53 vol% pyroxene, but with 17 vol% plagioclase/maskelynite and no mesostasis (Aoudjehane et al., 2012). The groundmass of Tissint has been highly fractured and, unlike Y98, is penetrated by numerous dark shock veins with black vesiculated glassy material.

Melt inclusions for Y98 and Tissint are typically circular to elliptical with diameters >5 to a few 10's of μm (Fig. 2). In some cases, melt inclusions have complex shapes, representing melt trapped between the interfaces of olivine grains. Many melt inclusions are intersected by cracks and fractures in the adjacent host olivine.

Daughter minerals can be found in some Y98 melt inclusions, although melt inclusions that are only glass ± sulfide droplets are more typical (Fig. 2C). Skeletal needles (Fig. 2D–F) of high-Ca pyroxene (En_{28-36} $Fs_{14-18}Wo_{50-56}$: Appendix 1 of the supplementary materials) are common daughter phases in Tissint melt inclusions. Large euhedral grains of Cr-spinel or chromite can be found along the walls of some melt inclusions (Fig. 2E), and appear to have impaired the advancing olivine interface and enhanced trapping of melt during olivine growth (e.g. Liu et al., 2013).

3. Analytical conditions

Trace elements were measured using the CAMECA ims1270 SIMS at UCLA. Polished samples and standards were gold-coated prior to analysis to avoid charging. Analyses used a primary oxygen beam of 20 nA and performed in mono-collection mode to employ ion imaging for targeting of inclusions. Sample points were pre-sputtered for 180 s. High intensity trace element peaks were monitored at ^{30}Si, ^{88}Sr, ^{89}Y, ^{91}Zr, ^{93}Nb, ^{137}Ba, ^{139}La, ^{140}Ce, ^{143}Nd, ^{149}Sm, ^{151}Eu, ^{156}Gd, ^{161}Dy, ^{168}Er, ^{172}Yb, ^{175}Lu at low mass resolution. Counting time per peak ranged between 2 to 3 s per cycle, with 5 cycles per analysis. High energy molecules were filtered by applying a 100 V offset to the extraction potential at a 50 eV bandpass. For high mass elements with low secondary ion intensities, peaks were monitored at ^{30}Si, ^{89}Y, ^{204}Pb, ^{206}Pb, ^{207}Pb, ^{208}Pb, ^{232}Th, and ^{238}U without energy offset and at High Mass Resolution (MRP ∼ 6000). Y was included to facilitate comparison with the energy-filtered analyses, and counting time per peak ranged between 3 to 10 s, with 5 cycles per analysis. The data were reduced using measured ^{30}Si intensities and the known SiO_2 wt% for the NIST 610, and USGS BHVO-2 and BCR-2 glass standards, and the measured SiO_2 wt% for glass locations following conventional procedures at UCLA (e.g., Schmitt and Simon, 2004). Precise measurement of U, and Th, however, proved particularly challenging due to their low concentrations (10–100 ppb). This is reflected by their 1σ errors, which exceed 100%, yielding little useful data. Original trace element analyses, prior to adjustment for secondary processes, are reported in Appendix 2, with 1σ error for trace element analyses in Appendix 3, and reference standard analyses in Appendix 4 of the supplementary materials.

Major element oxides of olivine, pyroxene, and glass were analyzed with the Cameca SX-100 EMPA at Johnson Space Center. The polished samples were carbon coated, following removal of gold coat. Standards included well-characterized natural and synthetic materials. Analytical conditions were 15 kV, 20 nA, 30–60 s count times, and a ~15 μm beam. Backscatter electron (BSE) image collection and X-ray mapping was performed using the field emission SEM JSM-7600F at Johnson Space Center. EMPA glass analyses were performed in the same location as their respective SIMS analysis. For a few glass locations, the presence of abundant olivine dendrites or where the width of glass between phenocrysts was less than the beam size, it is reasonable that the analytical volume encompassed multiple phases, generating mixed analyses and low EMPA totals. Attempts were made to avoid these problematic glass locations when possible. EMPA olivine analyses are reported in Appendix 5 of the supplementary materials, with glass analyses reported in Table 1a–c.

4. Electron microprobe characterization of glass and mineral phases

Melt inclusions in Y98 are associated with host olivine Fo$_{70-75}$ with an average of Fo$_{74}$. A similar pattern is observed for Tissint, with Fo$_{58-76}$, and an average of Fo$_{68}$. These observations are consistent with other studies, where melt inclusions are associated with olivine Fo$_{<75-77}$ (e.g. Basu Sarbadhikari et al., 2011; Liu et al., 2013).

Y98 melt inclusions have higher Mg# numbers (i.e. Mg# = Mg/[Mg + Fe] × 100, where Mg and Fe are molar %) relative to those in Tissint, with values up to Mg#$_{44}$ and an average of Mg#$_{37}$ (Table 1a). Y98 melt inclusions also have higher CaO and MgO wt%, and CaO/Al$_2$O$_3$ values compared to Tissint (Fig. 3A). The Y98 interstitial glass analyses have Mg#$_{5-15}$, with an average of Mg#$_{14}$ (Table 1b); consistent with quenching after olivine and low-Ca pyroxene crystallization. When plotted together, the Y98 melt inclusions and interstitial glass analyses form positive linear trends between Mg# vs. MgO wt%, CaO wt% (Fig. 3B), SiO$_2$ wt% (Fig. 3C), and negative linear trends between Mg# vs. FeO wt% (Fig. 3D), Al$_2$O$_3$ wt% (Fig. 3E), and S ppm. Relative to Y98, Tissint melt inclusions span a wider range of Mg# (Mg#$_{0.14-38}$), CaO wt%, and CaO/Al$_2$O$_3$ values (1.3 to 0.4), and have lower values for FeO and MgO wt%, and S concentration, while SiO$_2$ values are notably higher (62–73 wt% vs. 54–62 for Y98: Table 1c). These features are consistent with entrainment of primitive melts during closed system host crystallization of olivine and cpx ± opx, sulfide, and Cr-spinel.

5. Reconstruction of original melt trace element composition

The impact of crystallization on the trace element composition of the melt and melt inclusions, prior to and following olivine entrapment, was evaluated using the thermodynamic modeling software PETROLOG3 (Danyushevsky and Plechov, 2011). PETROLOG3 is specifically designed for modeling forward and reverse melt crystallization, and post-entrapment re-equilibration of olivine-hosted melt inclusions (Danyushevsky and Plechov, 2011). Conditions were set at fO$_2$ equal to iron-wustitie and pressures of 10 and 5 kbar, following the results of Y98 crystallization experiments by Rapp et al. (2013). The model selected for olivine calculation was the $K_{D\ Fe\text{-}Mg}^{Ol\text{-}Melt}$ equilibrium value 0.35 from Filiberto and Dasgupta (2011).

Crystallization models using bulk–rock compositions demonstrate the Y98 melt inclusions were trapped shortly around the appearance of low-Ca pyroxene. For Tissint, which experienced a longer cooling history, the timing of melt inclusion entrapment occurred after pyroxene crystallization. Post-entrapment re-equilibration modeling of melt inclusions in both Y98 and Tissint identifies ~30–40% by volume wall–rock olivine crystallization. For Tissint melt inclusions, the volume of secondary cpx crystallization was estimated at ~30–40%, using backscatter images and pixel counting. For these melt inclusions, their compositions were re-

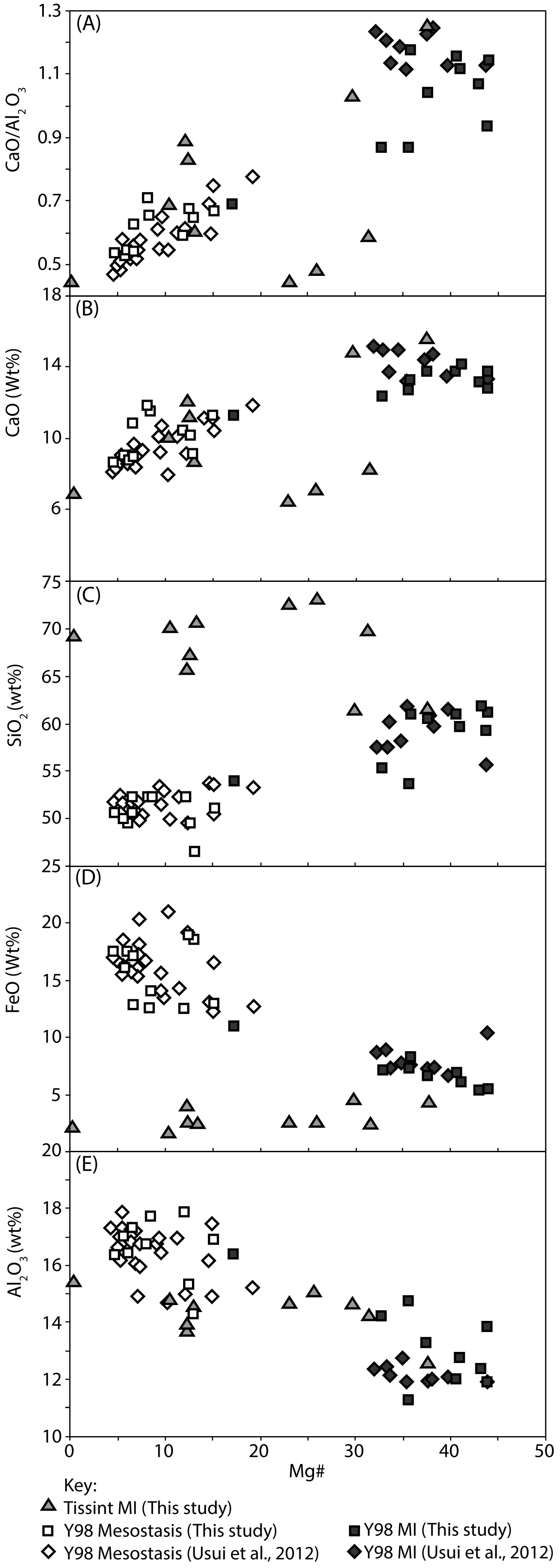

Fig. 3. Major element data vs. Mg#'s for olivine hosted melt inclusions and Y98 interstitial glass.

Table 1

Major and trace element composition of (a) olivine hosted melt inclusions in Y98, (b) the interstitial glass of Y98, and (c) olivine hosted melt inclusions in Tissint. Trace element concentrations have been adjusted to account for post-entrapment olivine and cpx crystallization.

a

	Y98MI1	Y98MI2	Y98MI3	Y98MI4	Y98MI5	Y98MI6	Y98MI7	Y98MI8
SiO_2	53.9	61.5	61.2	60.0	61.3	60.8	62.2	54.3
TiO_2	1.12	0.96	0.95	1.17	0.98	0.90	0.96	1.34
Al_2O_3	14.8	12.1	12.0	12.8	11.3	13.3	12.3	16.4
FeO	7.54	5.14	6.83	6.25	8.37	6.81	5.50	11.01
MnO	0.28	0.09	0.32	0.27	0.28	0.23	0.20	0.27
CaO	12.87	14.22	13.98	14.34	13.31	13.90	13.22	11.33
MgO	2.34	2.30	2.61	2.44	2.62	2.30	2.34	1.28
Na_2O	2.25	1.42	1.23	1.33	1.06	1.29	1.33	2.25
K_2O	0.10	0.05	0.04	0.03	0.07	0.09	0.07	0.09
Cr_2O_3	0.08	0.18	0.27	0.23	0.22	0.08	0.14	0.02
NiO	0.01			0.02	0.05	0.05	0.00	
SO_2	0.22	0.22	0.23	0.13	0.33	0.16	0.09	0.29
Sum	95.5	98.2	99.7	99.0	99.9	99.9	98.3	98.6
Mg#	35.6	44.4	40.5	41.0	35.8	37.6	43.1	17.2
CaO/Al_2O_3	0.87	1.17	1.16	1.12	1.18	1.05	1.08	0.69
La (ppm)	0.23	0.06	0.08	0.13		0.09		0.15
Ce	0.64	0.13	0.20	0.27		0.19		0.31
Nd	0.90	0.26	0.38	0.35		0.20		0.23
Sm	0.91	0.26	0.34	0.23		0.25		0.33
Eu	0.38	0.12	0.15	0.14		0.12		0.14
Gd	1.45	0.57	0.68	0.84		0.62		0.67
Tb		0.10	0.15	0.16		0.12		0.13
Dy	2.41	0.75	0.95	1.14		0.98		1.15
Er	1.51	0.47	0.69	0.69		0.49		0.89
Yb	2.15	0.59	0.69	0.74		0.69		1.11
Lu		0.06	0.09	0.14		0.10		0.12
Sr	25.8	6.3	9.5	8.0		8.6		14.4
Zr	20.4	8.2	8.7	13.5		11.3		28.8
Y	14.1	4.6	5.8	6.4		5.6		6.3
Ba	3.73	2.03	1.87	2.63		1.63		5.62
Nb	0.20	0.06	0.10	0.13		0.12		0.13
Pb	0.19	4.70			1.81	1.00	1.21	

b

	Y98 Glass1	Y98 Glass2	Y98 Glass3	Y98 Glass5	Y98 Glass6	Y98 Glass7	Y98 Glass8	Y98 Glass9	Y98 Glass10
SiO_2	49.7	52.4	50.7	50.7	52.1	50.1	49.6	52.2	46.8
TiO_2	1.56	0.97	1.01	1.08	1.18	1.18	1.24	1.04	1.18
Al_2O_3	15.3	17.7	16.3	16.4	17.3	17.1	16.4	17.9	14.3
FeO	18.60	14.14	17.47	17.15	12.90	16.14	17.40	12.66	18.59
MnO	0.40	0.42	0.31	0.44	0.41	0.36	0.37	0.40	0.41
CaO	10.26	11.62	8.76	8.93	10.89	9.04	8.91	10.57	9.24
MgO	1.50	0.73	0.49	0.64	0.52	0.55	0.63	0.96	1.55
Na_2O	1.92	2.02	2.74	2.34	2.56	2.25	2.35	2.46	2.43
K_2O	0.04	0.06	0.07	0.05	0.07	0.07	0.06	0.05	0.04
Cr_2O_3				0.03	0.02	0.02	0.01	0.02	0.05
NiO		0.03				0.02	0.03	0.05	
SO_2	0.69	0.34	1.01	0.53	0.34	0.30	1.28	0.29	0.49
Sum	99.9	100.4	99.0	98.3	98.3	97.1	98.3	98.6	95.0
Mg#	12.6	8.4	4.7	6.2	6.7	5.7	6.0	11.9	12.9
CaO/Al_2O_3	0.67	0.66	0.54	0.54	0.63	0.53	0.54	0.59	0.65
La (ppm)	0.47	0.42	0.48	0.51	0.36	0.47		0.43	0.46
Ce	1.40	1.12	1.30	1.30	1.06	1.40	0.98	0.99	1.26
Nd	1.87	1.62	1.87	2.01	1.91	1.92	1.29	1.47	1.77
Sm	1.42	1.37	1.77	1.37	1.37	1.42	1.04	0.96	1.12
Eu	0.78	0.69	0.86	0.98	0.82	0.88	0.58	0.59	0.65
Gd	3.29	2.70	2.91	3.17	3.01	3.11	2.02	2.93	2.60
Tb								0.64	0.58
Dy	4.63	4.06	4.20	4.02	4.71	4.55	3.31	4.08	4.60
Er	2.45	2.49	2.61	2.57	2.96	2.78	2.20	2.63	2.68
Yb	3.09	2.74	2.75	2.81	2.65	3.28	2.46	2.94	2.44
Lu								0.44	0.37
Sr	51.6	51.5	59.1	57.7	44.3			42.4	47.6
Zr	37.4	36.2	38.2	40.1	36.6			32.5	33.7
Y	25.8	22.8	24.9	24.8	25.9			24.5	23.8
Ba	5.10	5.39	5.41	5.18	4.79	5.12	6.09	4.51	4.36
Nb	0.62	0.51	0.62	0.59	0.56	0.66	0.49	0.53	0.47
Pb					0.24	0.23	0.42	0.24	

(*continued on next page*)

Table 1 (*continued*)

c

	Tissint MI2	Tissint MI3	Tissint MI4	Tissint MI5	Tissint MI6	Tissint MI7	Tissint MI10	Tissint MI11
SiO_2	69.9	69.2	67.5	70.2	61.7	61.6	65.9	72.7
TiO_2	1.38	0.97	1.67	1.08	1.45	1.21	1.14	1.09
Al_2O_3	14.2	15.4	13.6	14.7	12.5	14.6	13.8	14.7
FeO	2.46	2.34	2.66	1.74	4.36	4.61	4.12	2.57
MnO	0.08	0.11	0.17	0.12	0.13	0.12	0.12	0.10
CaO	8.44	6.90	11.36	10.19	15.66	15.08	12.32	6.55
MgO	0.64	0.00	0.21	0.11	1.47	1.10	0.32	0.43
Na_2O	2.08	2.23	1.41	1.53	1.32	0.91	1.68	2.08
K_2O	0.08	1.32	0.67	0.86	0.04	0.28	0.05	0.08
Cr_2O_3		0.03		0.00	0.04	0.02	0.25	
NiO				0.04	0.02	0.01	0.01	0.05
SO_2	0.08		0.06	0.12	0.03	0.00	0.07	0.01
Sum	99.3	98.6	99.3	100.7	98.7	99.5	99.8	100.4
Mg#	31.5	0.1	12.6	10.4	37.6	29.7	12.3	23.0
CaO/Al_2O_3	0.59	0.45	0.83	0.69	1.25	1.04	0.89	0.45
La (ppm)		0.22	0.15	0.16	0.21		0.28	0.14
Ce		0.67	0.54	0.46	0.72		0.88	0.50
Nd		0.92	0.90	0.63	1.14		1.03	0.74
Sm		0.74	0.70	0.47	0.48		0.71	0.51
Eu		0.28	0.24	0.23	0.27		0.41	0.34
Gd		1.21	1.06	0.76	1.20		1.53	1.00
Tb		0.25	0.25	0.20	0.28		0.31	0.29
Dy		1.64	1.59	1.22	1.46		2.15	1.46
Er		0.99	1.30	0.66	0.99		1.07	0.84
Yb		1.19	0.91	0.67	1.13		1.07	0.88
Lu		0.11	0.10	0.06	0.14		0.13	0.10
Sr		22.4	19.7	16.0	23.3		27.1	25.1
Zr		15.0	16.1	10.9	17.0		19.4	18.8
Y		9.3	9.0	6.6	9.3		11.2	8.8
Ba		1.48	0.78	1.04	1.19		1.41	1.12
Nb		0.15	0.08	0.08	0.12		0.17	0.10
Pb		0.20	0.22	0.16	0.31			

calculated to add back the volume of cpx prior to post-entrapment re-equilibration modeling.

Trace elements analyzed in the study are all highly incompatible in olivine (and opx), generally $D_i^{\text{mineral/melt}} << 0.01$ (e.g. Kennedy et al., 1993). For cpx, $D^{\text{cpx/melt}}$ values can be an order of magnitude higher, generally >0.01, with almost all elements being moderately incompatible (e.g. Johnson, 1998). Adjustments for pre- and post-entrapment olivine and cpx crystallization, using the results of PETROLOG3, resulted in a decrease in the trace element concentration (Table 1a–c; Fig. 4) due to the reduction in melt volume with mineral crystallization, but generated no significant change (i.e. do not exceed the errors on analyses) for ratios of moderately incompatible to highly incompatible elements in cpx, (i.e. Zr/Nb).

5.1. *Diffusive melt inclusion re-equilibration during cooling*

Olivine-hosted melt inclusions exhibit rapid secondary melt Fe–Mg re-equilibration and post-entrapment diffusive exchange with their host and daughter phases during slow cooling (e.g. Danyushevsky et al., 2000; Gaetani and Watson, 2000). While traditionally assumed immobile on magmatic timescales, recent observations have shown incompatible trace elements (i.e. REE) in olivine to behave in a similar manner during cooling (e.g. Spandler and O'Neill, 2010). In contrast, however, Cherniak (2010) reports melt-olivine REE diffusion values that are over three orders of magnitude slower to those of Spandler and O'Neill (2010). These conflicting studies support the need for a greater understanding of incompatible element mobility in olivine, leaving the potential for secondary trace element re-equilibration unresolved.

5.2. *The influence of terrestrial alteration and contamination*

Although Y98 experienced impact shock and displays abundant fracture networks (Greshake et al., 2004), there exists no petrographic evidence to support infiltration of terrestrial fluids during residence on the Antarctic ice (i.e. iron oxides and hydroxides, Ca–Fe–K sulfates and other evaporates, clay weathering products, silica and carbonate precipitates, dissolution of phosphates and glasses: e.g. Crozaz et al., 2003). The mobilization of LREE in Antarctic meteorites is typically associated with dissolution of calcium phosphates; a rich source of REE (i.e. Crozaz et al., 2003). Y98, however, contains no phosphates or other trace element enriched phases. Despite spot analysis locations chosen to spatially characterize its composition, the Y98 interstitial glass is remarkably homogeneous (Figs. 4A and 5A), lacking evidence to suggest post-magmatic alteration. For their olivine-hosted melt inclusions, Usui et al. (2012), using the same Y98 thin section, report constant ratios of H_2O/F, Cl/F, and S/F, supporting them to have remained closed to terrestrial alteration during residence on the Antarctic ice.

In contrast to Y98, Tissint was collected soon after falling, and terrestrial contamination is not expected. Despite this, Aoudjehane et al. (2012) report an LREE enriched component, with a small but resolvable Ce anomaly (indicating hydrothermal oxidation of Ce^{+3} to Ce^{+4}), in the Tissint impact glass. This is proposed to represent the impact of martian surface weathering and fluid infiltration. Barrat et al. (2014), however, observe no exotic LREE component in their Tissint impact melt analyses. The degree to which any surface component may have penetrated the matrix of Tissint, prior to or during impact melting, is also not immediately clear. Melt inclusions reported here, however, parallel their LREE-depleted whole-rock values (Fig. 4c; Aoudjehane et al., 2012), and display no evidence for LREE contamination or heterogeneity among other fluid mobile elements (Figs. 4C and 5C).

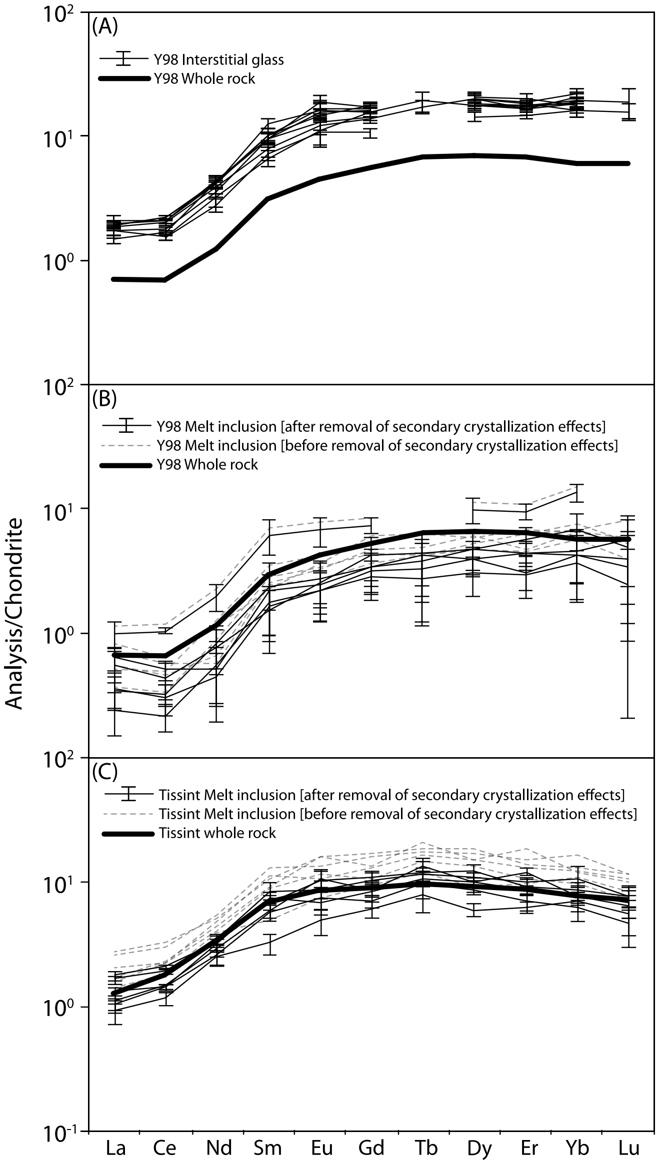

Fig. 4. Chondrite normalized REE profiles. Y98 whole rock REE data from Shirai and Ebihara (2004), and Aoudjehane et al. (2012) for Tissint.

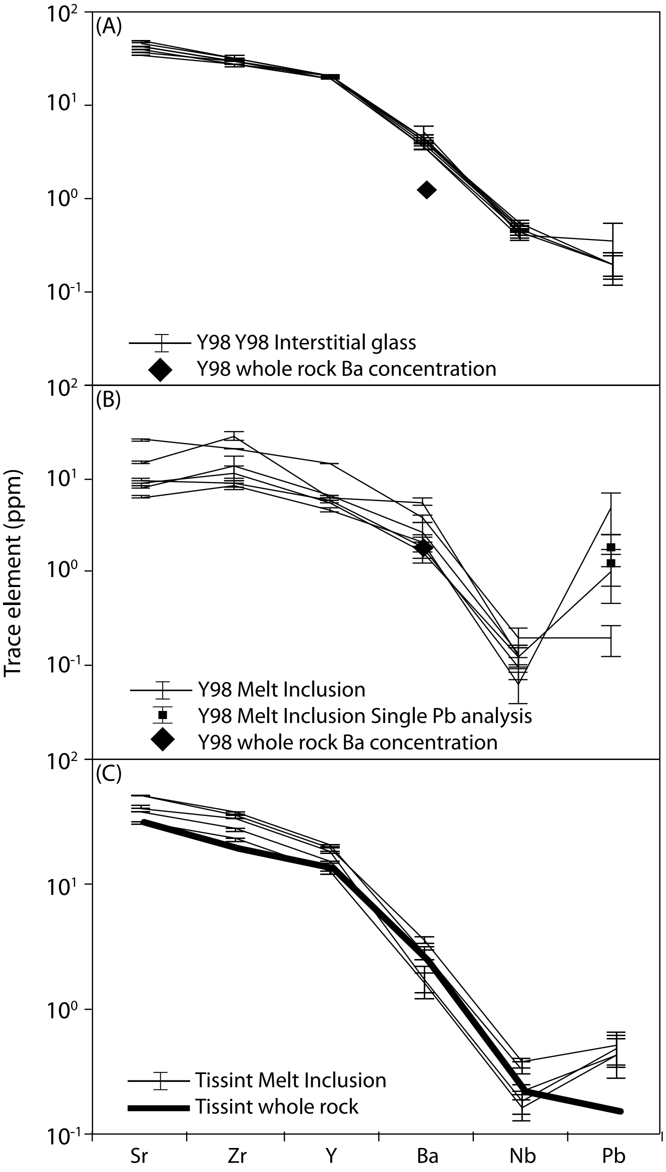

Fig. 5. Calculated parental melt inclusion trace element concentration. Elements are arranged in their order of decreasing concentration from Sr to Pb. Error bars are 1σ error. Y98 whole rock REE data from Shirai and Ebihara (2004), and Aoudjehane et al. (2012) for Tissint.

6. The most primitive trace element records observed in depleted shergottites are recorded in their olivine-hosted melt inclusions

Chondrite-normalized REE profiles for both Y98 and Tissint melt inclusions, and the Y98 interstitial glass, are characteristically LREE depleted and parallel those of their host rock (Shirai and Ebihara, 2004; Aoudjehane et al., 2012; Fig. 4). For Y98, the interstitial glass REE profiles plot above their whole rock (Fig. 4A), as expected. The Y98 melt inclusion REE profiles plot close to, but below the Y98 whole-rock value (Fig. 4B), while the Tissint melt inclusion REE profiles overlap with their whole rock.

It is expected that melt inclusion REE profiles should overlap with their whole rock profile, assuming closed system behavior. The scatter in absolute elemental concentrations likely reflects uncertainties with secondary olivine and cpx crystallization volume estimates and spot specific dilution with sputtering variable proportions of daughter phases or the olivine host (Fig. 2).

Importantly, REE profiles for Y98 display a flattening between La and Ce (Fig. 4A, B), where La values plot above the LREE profiles expected with melt depletion. This feature is not clearly observed in the REE profiles for Tissint melt inclusions (Fig. 4C), however, they do display a concave MREE-HREE profile, peaking between Gd–Tb–Dy (Fig. 4C), consistent with a residual garnet mantle mineralogy.

A comprehensive list of trace elements has yet to be produced for the whole Y98 composition, limiting comparisons with melt inclusion and interstitial glass analyses. The concentration of Ba in the interstitial glass is 3 to 4 times higher than the whole rock value (Fig. 5A), while the melt inclusions broadly overlap (Fig. 5B) (Shirai and Ebihara, 2004). Y, Zr, and Sr concentrations in the Y98 melt inclusions range between ∼2 to 15 ppm, while Nb is 0.13 to 0.03 ppm (Fig. 5B); consistent with a melt depleted mantle source. Trace element concentrations in Tissint melt inclusions (Fig. 5C) are elevated relative to those in Y98, and overlap with values reported for their whole rock (Aoudjehane et al., 2012). Identical to Y98, the highly incompatible elements Ba and Nb have the lowest concentrations (average Ba = 1.17 ppm, Nb = 0.12 ppm), relative to the moderately incompatible elements Y, Zr, and Sr (average Zr = 16 ppm, Sr = 22 ppm), in Tissint melt inclusions.

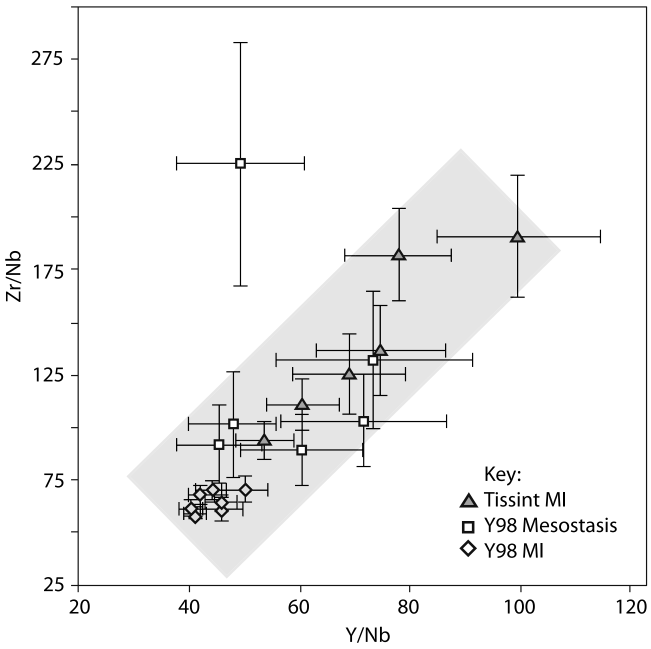

Fig. 6. Plot Y98 and Tissint melt inclusion, and Y98 ground mass glass Zr/Nb vs. Y/Nb values.

Zr/Y values display very little variability between Y98 melt inclusions (Zr/Y = 1.3 to 2.3, with one at 4.5), Y98 interstitial glass (Zr/Y = 1.33 to 1.62), and Tissint melt inclusions (Zr/Y = 1.75 to 2.34), indicating a coupled partitioning behavior during melting and crystallization. In contrast, Y/Nb and Zr/Nb values are variable between the three glass analyses (Fig. 6), reflecting the highly incompatible behavior of Nb in a cpx-garnet bearing mantle source.

Both Y98 and Tissint melt inclusions have elevated and variable Zr/Nb values (Tissint = 94 to 192, Y98 = 93 to 225). The whole rock Tissint Zr/Nb value (83 to 90) falls just below its lowest melt inclusion value (TissintMI3 = 98). Similarly, despite no whole rock Zr and Nb data, the Y98 interstitial glass analyses have lower and restricted Zr/Nb values (60 to 71) relative to their melt inclusions. Interestingly, a few melt inclusion analyses display Zr/Nb values that exceed the QUE 94201 whole rock value (Zr/Nb = 147).

The origin of this melt inclusion diversity is not immediately clear, and the occurrence of Zr/Nb values greater than that reported for QUE 94201 may have important implications on the nature of the depleted mantle. What is clear, for at least Y98, is that the melt inclusion analyses display a greater magnitude of trace-element heterogeneity than their groundmass glass. This could be explained as evidence for polybaric melt accumulation, prior to mixing and averaging of the whole rock composition.

For the Y98 melt inclusions, Pb concentrations range between 0.11 to 2.17 ppm (Fig. 5B). Interestingly, the single Pb enriched melt inclusion also contains a small sulfide at the surface, which was sputtered along with its host glass (Fig. 2C). This supports Pb to have been preferentially partitioned into these sulfides, forming Pb hotspots amongst Pb depleted glasses. The high abundance of sulfides in the mesostasis may help explain why Pb concentrations in the Y98 interstitial glasses are lower than the melt inclusions (0.24 to 0.25 ppm Pb, with one at 0.42 ppm: Fig. 5A); a trend opposite to all other elements. Tissint melt inclusions display a narrower range of Pb concentrations, 0.16 to 0.32 ppm Pb (Fig. 5C), which overlap with those reported for the whole rock (0.15 to 0.25 ppm: Aoudjehane et al., 2012).

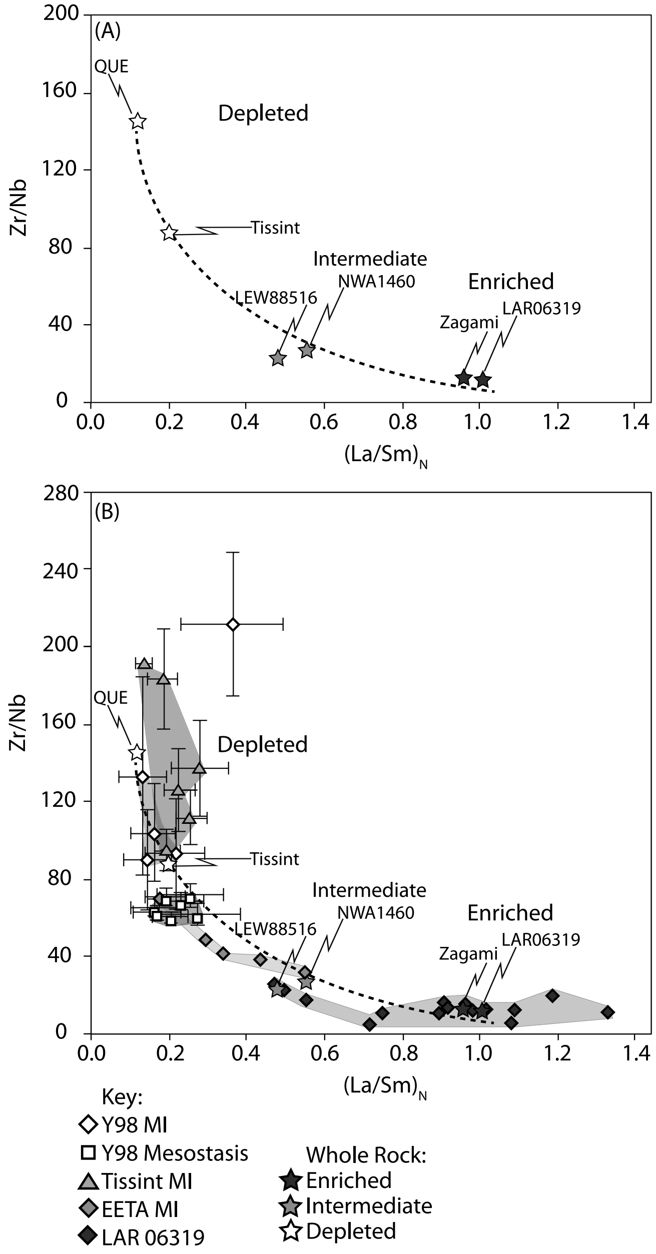

Fig. 7. (A) εNd vs (La/Sm)$_N$ (where N denotes a chondrite normalized ratio), and (B) Zr/Nb, for whole rock shergottite meteorites. (C) Zr/Nb vs. (La/Sm)$_N$ and (D) Zr/Nb vs. Nb/Y, for the interstitial glass of Y98, and olivine-hosted melt inclusions analyses from two depleted shergottites, Y98 and Tissint, an intermediate shergottite EETA 79001 Lith-C (Liu et al., 2013), and an enriched shergottite LAR06319 (Basu Sarbadhikari et al., 2011). Error bars for our analyses are 1σ. See Fig. 1 for whole rock data references.

7. Comparison with the shergottite suite and the generation of compositional heterogeneity

The extended Sr–Nd radiogenic isotope array for the shergottite meteorites (Fig. 1) is considered to represent mixing between depleted mantle melts and an enriched component (e.g. Borg et al., 1997). Tissint and Y98 plot close to QUE 94201 (Fig. 1) (Borg et al., 1997), but along the trend towards slight isotopic and trace element enrichment.

Unlike Y98 and Tissint, QUE 94201 is an olivine-free, maskelynite and pyroxene bearing sample (e.g. Borg et al., 1997). While not petrographically primitive, QUE 94201 is one of the most isotopically primitive amongst the LREE depleted shergottites, with a Sm–Nd age of 327 ± 19 Ma, an initial ^{87}Sr/^{86}Sr value of 0.701298,

εNd = +48 and εHf = +43, and is the best characterized representation of an uncontaminated melt from the depleted shergottite mantle (e.g. Borg et al., 1997; Blichert-Toft et al., 1999). The enriched end-member is defined by shergottites such as NWA 4468, Zagami, and the olivine-phyric Larkman Nunatak (LAR) 06319 (Fig. 1). They display broadly flat REE profiles, an initial ^{87}Sr/^{86}Sr value of > 0.72100, εNd $\cong -7$ (Fig. 1), and are generally younger than the depleted shergottites with ages ~160 to 190 Ma (e.g. Nyquist et al., 2001; Usui et al., 2010).

On a plot of whole rock shergottite Zr/Nb vs. $(\text{La/Sm})_N$ (Fig. 7A), a hyperbolic relationship is observed, similar to that seen with radiogenic isotopes (i.e. Fig. 1). These ratios allow a comparison between melt inclusion and whole rock trace element analyses, which in turn permit connections to be drawn between the melt inclusion data and the isotopic sources represented by the shergottites.

In Fig. 7B, data from this study is plotted atop whole rock data, along with trace element analyses for olivine-hosted melt inclusions from enriched olivine phyric shergottite LAR (Basu Sarbadhikari et al., 2011) and intermediate olivine phyric shergottite EETA Lith-A (Liu et al., 2013). It is clear that trace element diversity in the melt inclusions for these four olivine-phyric shergottites covers the entire array generated by the whole rock analyses. These coupled relationships suggest that fractionation of incompatible trace elements accompanies systematic trends in their isotopic diversity, and that the generation of geochemical heterogeneity occurs early in the magmatic history of the shergottites; i.e. during partial melting or immediately upon migration from their respective source.

8. Origin of depleted and enriched end members

8.1. Partial melting and original depletion of the shergottite mantle

Mantle melting models, the majority of which use the diverse Sm–Nd, Rb–Sr (i.e. Fig. 1), and Lu–Hf shergottite meteorite isotope trends (e.g. Borg et al., 1997; Borg and Draper, 2003; Shih et al., 2005; Debaille et al., 2008; Symes et al., 2008; Blinova and Herd, 2008), posit that the shergottite mantle experienced at least two melting events. One is thought to have occurred soon after magma ocean crystallization and mantle differentiation, and another at a time close to the final stage of melting and shergottite formation (Borg et al., 1997; Debaille et al., 2008); although the specific timing and number of melting events remains uncertain.

The mantle melting model presented here follows a fractional fusion approach, calculating an approximate mantle source composition for the depleted shergottites through extraction of melt from an initially undifferentiated source. The generation of a final depleted shergottite mantle source (C_i^m) is calculated through mass balance using the batch melting equation (Eq. (1)):

$$C_i = \frac{C_o}{F + D_i\,(1 - F)}, \tag{1}$$

where, $C_i^m = F - (C_i \times F)$, F is the melt fraction, D_i is the mineral/melt distribution coefficient for element i, C is the concentration of element i in the melt, and C_o is the concentration of element i in the source.

The final depleted shergottite mantle is assumed to be capable of generating trace element features in shergottite QUE 94201, while the initial post-accretion shergottite mantle (or magma ocean) is assumed to have a carbonaceous chondritic (CI) composition. This approach follows that of Borg and Draper (2003), although a starting composition based on magma ocean crystallization models is not used due to uncertainties in the depth of melting during shergottite formation, the source mineralogy, mechanism of crystal accumulation and cumulate formation, number and timing of melting events, and mineral-melt partition coefficients.

8.2. Melting in the martian mantle

During melting, the HFSE and REE systematics of the melt and residual mantle are controlled principally by garnet and pyroxene. $D_{\text{Zr/Nb}}^{\text{Mineral/melt}}$ values are similar for both garnet and pyroxene ($D_{\text{Zr/Nb}}^{\text{cpx}} \sim 15$ and $D_{\text{Zr/Nb}}^{\text{grt}} \sim 14$), and for a given melt fraction, the magnitude of Zr/Nb fractionation generated during melting will be similar (Fig. 8). In contrast, $D_{\text{La/Sm}}^{\text{Mineral/melt}}$ values vary from 0.318 for cpx, to 0.058 for garnet; a result of the decreasing incompatibly of the REE from LREE to MREE, and compatibility of HREE in garnet.

A number of estimates have been made to determine the residual mineralogy of the shergottite mantle during shergottite generation; however, uncertainty persists (e.g. Jones, 1989; Longhi and Pan, 1989; Longhi et al., 1992; Blichert-Toft et al., 1999; Borg and Draper, 2003; Debaille et al., 2008). Modeling here began with the compiled mineral proportions, cpx 18.4%, opx 28.6%, olivine 42.6%, garnet 10.4%, from Blinova and Herd (2008), and partition coefficients from McDade et al. (2003), Tuff and Gibson (2007), chosen to best represent melting conditions in a deep Fe enriched mantle.

In their models, Borg and Draper (2003) calculated the composition of ol + pyx + garnet cumulate piles generated during magma ocean crystallization, and compared the composition of melts from these piles to QUE 94201. While successful at reproducing many features, their model could not generate the required degree of LREE depletion, which they admit.

To generate the low La/Sm values (i.e. LREE depletion) in QUE 94201 (Fig. 8), the best model fit is observed here when cpx is exhausted first and garnet remains until final formation of the QUE 94201 source (Fig. 8), supporting at least two prior mantle melting events: (1) to exhaust cpx, and (2) to fractionate the LREE in the presence of residual garnet. This observation, however, is only a first order solution to the complex evolution of the martian mantle. In reality, the composition of mineral phases, and the resulting bulk mantle composition at a particular depth, will reflect an equilibrium relationship with a fractionating magma ocean composition during a complex mantle crystallization sequence (e.g. Borg and Draper, 2003). Although incompatible element modeling here favors a mantle source that has exhausted its cpx, the olivine-phyric shergottites, and shergottite suite as a whole, contain abundant cpx. It may be reasonable for a portion of cpx to remain in the source during formation of the shergottite melts, but this cpx is sufficiently depleted in incompatible elements, relative to garnet, as to not hold a significant controlling influence over these elements during partial melting. Shih et al. (2005) and Blinova and Herd (2008) discuss similar models as three-stage mantle melting models involving an intermediate melting event that produces a Nakhlite-like parental melt and cpx depleted, or exhausted, mantle residue.

The importance of residual garnet in the depleted shergottite mantle has been proposed previously to explain the degree of LREE depletion (e.g. Gleason et al., 1996), elevated ^{147}Sm/^{143}Nd values (e.g. Borg et al., 1997; Shih et al., 2005), and ^{177}Lu–^{176}Hf composition (e.g. Blichert-Toft et al., 1999). However, the role of garnet in the martian mantle is somewhat complicated. A characteristic of shergottite meteorites is their Al depletion and superchondritic $\text{CaO/Al}_2\text{O}_3$ values (~1.0–1.5: i.e. Longhi and Pan, 1989; Agee and Draper, 2004). Shergottite crystallization experiments show that the Al depletion cannot be resolved by mantle melting with a residual aluminous phase (plagioclase, spinel, or garnet) or fractional crystallization of an aluminous phase (Longhi and Pan, 1989).

Martian mantle melting experiments have successfully generated Al depleted melts with super-chondritic $\text{CaO/Al}_2\text{O}_3$ values only at low-degrees of melting, close to the solidus, when garnet

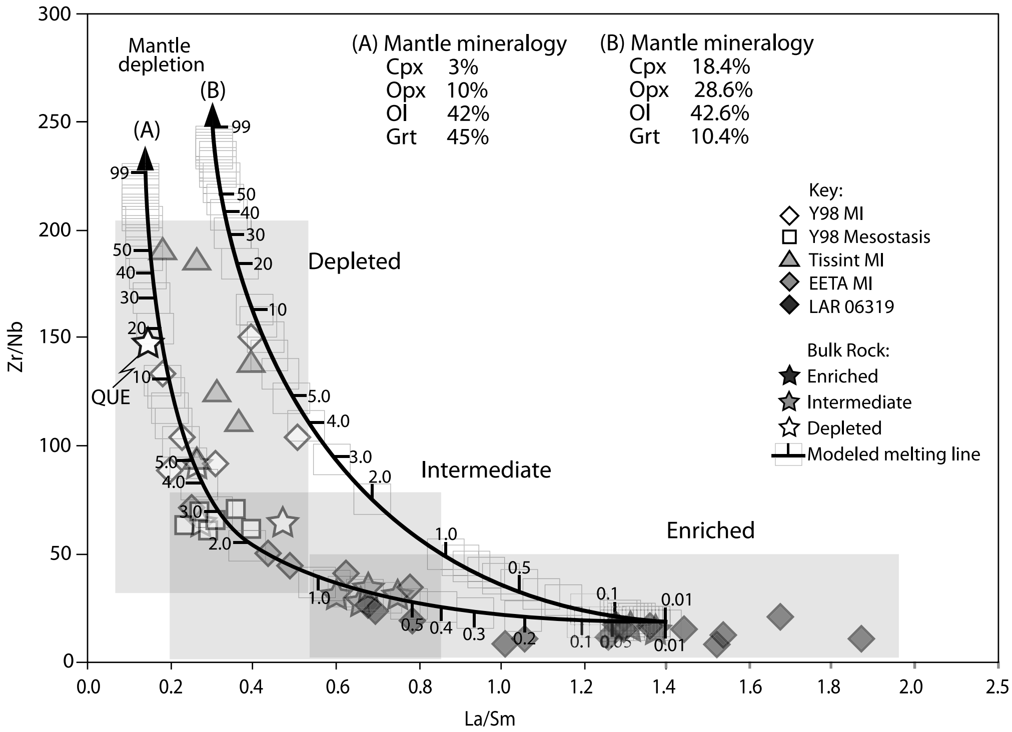

Fig. 8. Zr/Nb vs. La/Sm for the shergottite meteorites. Included are whole rock shergottite compositions, olivine host melt inclusions for Y98, Tissint, EETA-Lith A (Liu et al., 2013), LAR06319 (Basu Sarbadhikari et al., 2011), and the interstitial glass of Y98 (see key). Dash marks on the fractional fusion lines (solid black lines) represent the % of melt that has been removed from the mantle. See text for detailed description. The mineral-melt partition coefficients and starting composition used during modeling are listed in Appendix 7 of the supplementary materials.

was residual (Bertka and Holloway, 1994; Agee and Draper, 2004; Matsukage et al., 2013); i.e. pressures >4.5 GPa (Matsukage et al., 2013). These primary melts, however, are enriched in FeO, depleted in SiO_2 and Al_2O_3, and match no known shergottite compositions.

8.3. *Location of the enriched reservoir*

The flattened chondrite normalized La–Ce trend for Y98 (Fig. 4A, B) is a feature observed in other depleted shergottites (e.g. Shih et al., 1982; Barrat et al., 2001), and common to terrestrial oceanic basalts and peridotites associated with metasomatism or assimilation of overlying crust (e.g. Menzies and Hawkesworth, 1987). The origin of this La enrichment in martian shergottites is likely linked to the involvement of an ancient and isotopically enriched source, based on the correlation between increasingly evolved εNd values and LREE enrichment (i.e. increasing $(La/Sm)_N$ values) (Fig. 1). More importantly, the Y98 melt inclusion data supports La enrichment to have been inherited from its source or acquired prior to extensive melt crystallization. A similar conclusion was proposed for enriched olivine-phyric shergottite LAR 06316 (Basu Sarbadhikari et al., 2011) and intermediate olivine-phyric shergottite EETA 79001 (Liu et al., 2013).

For assimilation of trace-element enriched and oxidized ancient crust to occur prior to extensive crystallization, high temperatures and rates of assimilation are required (e.g. Kent et al., 2002). As noted previously, Y98 has a 1 bar liquidus temperature of ~1450 °C (Koizumi et al., 2004), indicating the olivine-phyric shergottite parental melts were particularly susceptible to contamination after leaving their source. Early crustal contamination is also favored when the assimilating component is either close to, or above, its solidus prior to melt–rock interaction, and when high temperature melts experiences rapid adiabatic ascent (i.e. during volcanic extrusion); leading to rapid consumption of the assimilating component with enhanced rates of thermal diffusion and the release of latent heat with melt crystallization (e.g. Huppert et al., 1984; Kent et al., 2002).

The presence of olivine megacrysts in the olivine-phyric shergottites suggests their parental melts experienced significant undercooling, possibly through having ascended rapidly from their source and subsequently encountered shallow crustal magma chambers or volcanic conduits (e.g. Usui et al., 2008; Welsch et al., 2013). If this were the case, early assimilation would have been aided by a large thermal gradient and thermal buffering with the prolonged release of latent heat during growth of olivine megacrysts (e.g. Settle, 1979; Wadhwa et al., 1994).

8.3.1. *Evidence for martian crustal recycling?*

The role of recycled crust in the martian mantle has been explored recently using experimental approaches as a means to understand shergottite geochemical diversity. Papike et al. (2013) demonstrate the LREE preferentially partition into phosphate phases (i.e. apatite, merrilite) after the transition of basalt to eclogite for a QUE 94201 starting composition. These phosphates are the first phases to melt during heating and may be responsible for LREE enrichment and geochemical diversity observed in the shergottite meteorites (Fig. 1). In a separate study, Tuff et al. (2013) demonstrate the disparate major element composition between martian surfaces analyses, performed at the Gusev crater by the Spirit rover, and martian meteorite samples, can be resolved through melting a Dreibus and Wanke (1985) bulk silicate Mars mantle under different fO_2 conditions. Tuff et al. (2013) propose the ~3.7 Ga old Gusev crater rocks require a more oxidized mantle than the younger meteorite samples, which could have been generated through early recycling of oxidized martian crust into the upper mantle (i.e. <120 km depth); analogues to subduction zones on Earth. The depleted shergottites represent melting of a deeper, reduced and garnet bearing mantle, while the enriched shergottites contain a greater contribution from the oxidized upper mantle.

In a recent study, Usui et al. (2012) report martian atmosphere hydrogen isotope signatures in the olivine-hosted melt inclusions of enriched olivine-phyric shergottite LAR 06319 (Shafer et al., 2010). This provides strong evidence that the source of the enriched component resides, or once resided, at close enough to the martian surface to interact with water in isotopic equilibrium with the martian atmosphere and/or hydrosphere; i.e. martian crust.

On Earth, hydrothermal alteration of oceanic crust is limited to just several km depth (e.g. Alt, 1995). Experimental work by Musselwhite et al. (2006) identified the Y98 parental melt segregated from its source at ∼100 km depth. The overlapping whole rock major element composition of other olivine-phyric shergottites (i.e. Tissint and the enriched shergottite LAR 06319) supports a similar depth of segregation to be expected. The observation in olivine-hosted melt inclusions of an enrichment in La, reported here for Y98, and martian atmosphere isotopic signatures, reported by Usui et al. (2012) for LAR 06319, suggests primitive depleted mantle melts either, (1) adiabatically ascended ∼ 90 km towards the martian surface without cooling or significant crystallization of olivine prior to assimilation of martian crust, or (2) during melt ascent, assimilated a martian crust component that had been recycled back into the upper mantle, close to the source of melting.

9. Summary and conclusions

Olivine-hosted melt inclusions in Y98 and Tissint, and the Y98 interstitial glass analyses, display chondrite-normalized REE profiles that parallel their whole rock REE profile. This suggests both Y98 and Tissint were closed systems during crystallization.

The Y98 melt inclusion REE profiles display a flattening between La and Ce. This feature represents the most primitive evidence of an enriched component in the magmatic history of a depleted shergottite mantle melt. This feature is not clearly observed for Tissint melt inclusions, however, they do display a slight depletion in their HREE relative to MREE, suggesting residual garnet in the mantle.

Element ratios of contrasting incompatibility for a typical olivine-pyroxene-garnet bearing mantle (i.e. Zr/Nb, Y/Nb, La/Sm) show significant diversity for the melt inclusion analyses; with a restricted range for the Y98 interstitial glass. The spread in element ratios for melt inclusion analyses possibly reflects the collection of small melt batches from a polybaric melt column. Combining element ratios with published olivine-hosted melt inclusion data from the intermediate olivine phyric shergottite 79001 Lith-A and enriched olivine phyric shergottite LAR 06319, a compositional array is generated which both parallels and extends beyond that produced by the whole rock shergottite analyses. This extended compositional array further supports geochemical and isotopic diversity between the shergottites to have been either inherited from their source, or incorporated early, prior to extensive host crystallization.

The origin of the depleted shergottite mantle end-member in this compositional array can be modeled during partial melting only if pyroxene is exhausted early in the mantle history. The loss of cpx leaves garnet to dominate the behavior of trace elements during subsequent melting events prior to final shergottite formation.

The origin of trace element enriched and isotopically evolved signatures represents either (1) assimilation during the final few km of melt ascent towards the martian surface with little to no cooling or significant crystallization of olivine prior to the assimilation of martian crust, or (2) assimilation soon after melt segregation, through melt–rock interaction with a portion of the martian crust recycled back into the mantle.

Acknowledgements

We are grateful to Dr. Anne Peslier at Johnson Space Center (JSC) for assistance with Electron Microprobe analyses (EMPA), and Dr. Kent Ross and Dr. Eve Berger for assistance with the JSC Field Emission Scanning Electron Microscope. Editorial handling and suggestions by Tamsin Mather, and comments by David Baratoux and Jon Wade, significantly improved upon the original manuscript. NASA funding comes from the Mars Fundamental Research Program (NNX11AF57G). The ion microprobe facility at UCLA is partly supported by a grant from the Instrumentation and Facilities Program, Division of Earth Sciences, National Science Foundation.

Appendix A. Supplementary material

Supplementary material related to this article can be found online at http://dx.doi.org/10.1016/j.epsl.2015.02.033.

References

Agee, C.B., Draper, D.S., 2004. Experimental constraints on the origin of Martian meteorites and the composition of the Martian mantle. Earth Planet. Sci. Lett. 224, 415–429. http://dx.doi.org/10.1016/j.epsl.2004.05.022.

Alt, J.C., 1995. Subseafloor processes in mid-ocean ridge hydrothermal systems. In: Humphris, Susan E., Zierenberg, Robert A., Mullineaux, Lauren S., Thomson, Richard E. (Eds.), Seafloor Hydrothermal Systems: Physical, Chemical, Biological, and Geological Interactions, vol. 91, pp. 85–114.

Aoudjehane, C.H., Avice, G., Barrat, J.-A., Boudouma, O., Chen, G., Duke, M.J.M., Franchi, I.A., Gattacceca, J., Grady, N.M., Greenwood, R.C., Herd, C.D., Hewins, R., Jambon, A., Marty, B., Rochette, P., Smith, C.L., Sautter, V., Verchosky, A., Webber, P., Zander, B., 2012. Tissint martian meteorite: a fresh look at the interior, surface, and atmosphere of Mars. Science 338, 785–788. http://dx.doi.org/10.1126/science.1224514.

Barrat, J.A., Blichert-Toft, J., Nesbitt, R.W., Keller, F., 2001. Bulk chemistry of Saharan shergottite Dar al Gani 476. Meteorit. Planet. Sci. 36, 23–29.

Barrat, J.A., Jambon, A., Ferrière, L., Bollinger, C., Langlade, J.A., Liorzou, C., Boudouma, O., Fialin, M., 2014. No Martian soil component in shergottite meteorites. Geochim. Cosmochim. Acta 125, 23–33. http://dx.doi.org/10.1016/j.gca.2013.09.033.

Basu Sarbadhikari, A., Goodrich, C.A., Liu, Y., Day, J., Taylor, L.A., 2011. Evidence for heterogeneous enriched shergottite mantle sources in Mars from olivine-hosted melt inclusions in Larkman Nunatak 06319. Geochim. Cosmochim. Acta 75, 6803–6820. http://dx.doi.org/10.1016/j.gca.2009.01.012.

Bertka, C.M., Holloway, J.R., 1994. Anhydrous partial melting of an iron-rich mantle I: subsolidus phase assemblages and partial melting phase relations at 10 to 30 kbar. Contrib. Mineral. Petrol. 115, 313–322. http://dx.doi.org/10.1007/BF00310770.

Blichert-Toft, J., Gleason, J.D., Télouk, P., Albarède, F., 1999. The Lu–Hf isotope geochemistry of shergottites and the evolution of the Martian mantle–crust system. Earth Planet. Sci. Lett. 173, 25–39. http://dx.doi.org/10.1016/S0012-821X(99)00222-8.

Blinova, A., Herd, C.D.K., 2008. Experimental study of polybaric REE partitioning between olivine, pyroxene and melt of the Y 980459 composition: insights into the petrogenesis of depleted shergottites. Geochim. Cosmochim. Acta 73, 3471–3492. http://dx.doi.org/10.1016/j.gca.2009.03.007.

Borg, L.E., Draper, D.S., 2003. A petrogenetic model for the origin and compositional variation of the Martian basaltic meteorites. Meteorit. Planet. Sci. 38, 1713–1731. http://dx.doi.org/10.1111/j.1945-5100.2003.tb00011.x.

Borg, L.E., Nyquist, L.E., Taylor, L.A., Wiesmann, H., Shih, C.-Y., 1997. Constraints on Martian differentiation processes from Rb–Sr and Sm–Nd isotopic analyses of the basaltic shergottite QUE 94201. Geochim. Cosmochim. Acta 61, 4915–4931. http://dx.doi.org/10.1016/S0016-7037(97)00276-7.

Bouvier, A., Blichert-Toft, J., Vervoort, J.D., Albarède, F., 2005. The age of SNC meteorites and the antiquity of the Martian surface. Earth Planet. Sci. Lett. 240, 221–233. http://dx.doi.org/10.1016/j.epsl.2005.09.007.

Bouvier, A., Blichert-Toft, J., Vervoort, J.D., Gillet, P., Albarède, F., 2008. The case for old basaltic shergottites. Earth Planet. Sci. Lett. 266, 105–124.

Bouvier, A., Blichert-Toft, J., Albarède, F., 2009. Martian meteorite chronology and the evolution of the interior of Mars. Earth Planet. Sci. Lett. 280, 285–295.

Brandon, A.D., Puchtel, I.S., Walker, R.J., Day, J., Irving, A.J., Taylor, L.A., 2012. Evolution of the martian mantle inferred from the ^{187}Re^{187}Os isotope and highly siderophile element abundance systematics of shergottite meteorites. Geochim. Cosmochim. Acta 76, 206–235. http://dx.doi.org/10.1016/j.gca.2011.09.047.

Cherniak, D.J., 2010. REE diffusion in olivine. Am. Mineral. 95, 362–368. http://dx.doi.org/10.2138/am.2010.3345.

Crozaz, G., Floss, C., Wadhwa, M., 2003. Chemical alteration and REE mobilization in meteorites from hot and cold deserts. Geochim. Cosmochim. Acta 67, 4727–4741. http://dx.doi.org/10.1016/j.gca.2003.08.008.

Danyushevsky, L.V., Plechov, P., 2011. Petrolog3: integrated software for modeling crystallization processes. Geochem. Geophys. Geosyst. 12, Q07021. http://dx.doi.org/10.1029/2011GC003516.

Danyushevsky, L.V., Della-Pasqua, F.N., Sokolov, S., 2000. Re-equilibration of melt inclusions trapped by magnesian olivine phenocrysts from subduction-related magmas: petrological implications. Contrib. Mineral. Petrol. 138, 68–83. http://dx.doi.org/10.1007/PL00007664.

Debaille, V., Yin, Q.-Z., Brandon, A.D., Jacobsen, B., 2008. Martian mantle mineralogy investigated by the $^{17}_{6}$Lu–^{176}Hf and ^{147}Sm–^{143}Nd systematics of shergottites. Earth Planet. Sci. Lett. 269, 186–199. http://dx.doi.org/10.1016/j.epsl.2008.02.008.

Dreibus, G., Wanke, H., 1985. Mars, a volatile-rich planet. Meteoritics 20, 367–381.

Filiberto, J., Dasgupta, R., 2011. Fe^{2+} Mg partitioning between olivine and basaltic melts: applications to genesis of olivine-phyric shergottites and conditions of melting in the Martian interior. Earth Planet. Sci. Lett. 304, 527–537. http://dx.doi.org/10.1016/j.epsl.2011.02.029.

Gaetani, G.A., Watson, E.B., 2000. Open system behavior of olivine-hosted melt inclusions. Earth Planet. Sci. Lett. 183, 27–41. http://dx.doi.org/10.1016/S0012-821X(00)00260-0.

Gleason, J.D., Kring, D.A., Boynton, W.V., 1996. The role of garnet in Martian mantle evolution: further evidence from shergottite rare earth patterns. In: 27th Lunar and Planetary Institute Science Conference. Abstract #1213.

Greshake, A., Fritz, J., Stöffler, D., 2004. Petrology and shock metamorphism of the olivine-phyric shergottite Yamato 980459: evidence for a two-stage cooling and a single-stage ejection history. Geochim. Cosmochim. Acta 68, 2359–2377. http://dx.doi.org/10.1016/j.gca.2003.11.022.

Huppert, H.E., Sparks, R.S.J., Turner, J.S., Arndt, N.T., 1984. Emplacement and cooling of komatiite lavas. Nature 309, 19–22. http://dx.doi.org/10.1038/309019a0.

Johnson, K.T.M., 1998. Experimental determination of partition coefficients for rare earth and high-field-strength elements between clinopyroxene, garnet, and basaltic melt at high pressures. Contrib. Mineral. Petrol. 133, 60–68. http://dx.doi.org/10.1007/s004100050437.

Jones, J.H., 1989. Isotopic relationships among the shergottites, the nakhlites and Chassigny. In: Proceedings of the 19th Lunar and Planetary Science Conference, pp. 465–474.

Kennedy, A.K., Lofgren, G.E., Wasserburg, G.J., 1993. An experimental study of trace element partitioning between olivine, orthopyroxene and melt in chondrules: equilibrium values and kinetic effects. Earth Planet. Sci. Lett. 115, 177–195. http://dx.doi.org/10.1016/0012-821X(93)90221-T.

Kent, A.J.R., Baker, J.A., Wiedenbeck, M., 2002. Contamination and melt aggregation processes in continental flood basalts: constraints from melt inclusions in Oligocene basalts from Yemen. Earth Planet. Sci. Lett. 202, 577–594. http://dx.doi.org/10.1016/S0012-821X(02)00823-3.

Koizumi, E., Mikouchi, T., McKay, G., Monkawa, A., Chokai, J., Miyamoto, M., 2004. Yamato980459: crystallization of Martian magnesian magma. In: 35th Lunar and Planetary Science Conference. Abstract #1494.

Le Bas, M.J., 2000. IUGS reclassification of the high-Mg and picritic volcanic rocks. J. Petrol. 41, 1467–1470. http://dx.doi.org/10.1093/petrology/41.10.1467.

Liu, Y., Balta, J.B., Goodrich, C.A., McSween Jr., H.Y., Taylor, L.A., 2013. New constraints on the formation of shergottite Elephant Moraine 79001 lithology A. Geochim. Cosmochim. Acta 108, 1–20. http://dx.doi.org/10.1016/j.gca.2013.01.008.

Longhi, J., Knittle, E., Holloway, J.R., Waenke, H., 1992. The bulk composition, mineralogy and internal structure of Mars. In: Kieffer, H.H., Jakosky, B.M., Snyder, C.W., Matthews, M.S. (Eds.), Mars. University of Arizona Press, pp. 184–208.

Longhi, J., Pan, V., 1989. The parent magmas of the SNC meteorites. In: Proceedings of the 19th Lunar and Planetary Science Conference Proceedings, pp. 451–464.

Matsukage, K.N., Nagayo, Y., Whitaker, M.L., Takahashi, E., Kawasaki, T., 2013. Melting of the Martian mantle from 1.0 to 4.5 GPa. J. Mineral. Petrol. Sci. 108, 201–214. http://dx.doi.org/10.2465/jmps.120820.

McDade, P., Blundy, J.D., Wood, B.J., 2003. Trace element partitioning on the Tinaquillo Lherzolite solidus at 1.5 GPa. Phys. Earth Planet. Inter. 139, 129–147. http://dx.doi.org/10.1016/S0031-9201(03)00149-3.

McSween, H.Y., Treiman, A.H., 1998. Martian meteorites. Rev. Mineral. Geochem. 36, 6.1.

Menzies, M.A., Hawkesworth, C.J. (Eds.), 1987. Mantle Metasomatism. Academic Press Geology Series. Academic Press INC, London.

Musselwhite, D.S., Dalton, H.A., Kiefer, W.S., Treiman, A.H., 2006. Experimental petrology of the basaltic shergottite Yamato-980459: implications for the thermal structure of the Martian mantle. Meteorit. Planet. Sci. 41, 1271–1290. http://dx.doi.org/10.1111/j.1945-5100.2006.tb00521.x.

Nyquist, L.E., Bogard, D.D., Shih, C.-Y., Greshake, A., Stöffler, D., Eugster, O., 2001. Ages and geologic histories of Martian meteorites. In: Kallenbach, R., Geiss, J., Hartman, W.K. (Eds.), Chronology and Evolution of Mars. Springer, Netherlands, pp. 105–164.

Papike, J.J., Burger, P.V., Shearer, C.K., McCubbin, F.M., 2013. Experimental and crystal chemical study of the basalt–eclogite transition in Mars and implications for martian magmatism. Geochim. Cosmochim. Acta 104, 358–376. http://dx.doi.org/10.1016/j.gca.2012.11.007.

Rapp, J.F., Draper, D.S., Mercer, C.M., 2013. Anhydrous liquid line of descent of Yamato-980459 and evolution of Martian parental magmas. Meteorit. Planet. Sci. 48, 1780–1799. http://dx.doi.org/10.1111/maps.12197.

Schmitt, A.K., Simon, J.I., 2004. Boron isotopic variations in rhyolites from Long Valley, California: recycling of hydrothermally altered intrusive margins. Contrib. Mineral. Petrol. 146, 590–605. http://dx.doi.org/10.1007/s00410-003-0514-6.

Settle, M., 1979. Lava rheology: thermal buffering produced by the latent heat of crystallization. In: Proceedings of the 10th Lunar and Planetary Science Conference, pp. 1107–1109.

Shafer, J.T., Brandon, A.D., Lapen, T.J., Righter, M., Peslier, A.H., Beard, B.L., 2010. Trace element systematics and ^{147}Sm–^{143}Nd and ^{176}Lu–^{176}Hf ages of Larkman Nunatak 06319: closed-system fractional crystallization of an enriched shergottite magma. Geochim. Cosmochim. Acta 74, 7307. http://dx.doi.org/10.1016/j.gca.2010.09.009.

Shih, C.-Y., Nyquist, L.E., Bogard, D.D., McKay, G.A., Wooden, J.L., Bansal, B.M., Wiesmann, H., 1982. Chronology and petrogenesis of young achondrites, Shergotty, Zagami, and ALHA77005: late magmatism on a geologically active planet. Geochim. Cosmochim. Acta 46, 2323–2344. http://dx.doi.org/10.1016/0016-7037(82)90205-8.

Shih, C.-Y., Nyquist, L.E., Park, J., Agee, C.B., 2014. Sm–Nd and Rb–Sr isotopic systematics of a heavily shocked Martian meteorite Tissint and petrogenesis of depleted shergottites. In: 45th Lunar and Planetary Science Conference. Abstract #1184.

Shih, C.-Y., Nyquist, L.E., Wiesmann, H., Reese, Y., Misawa, K., 2005. Rb–Sr and Sm–Nd dating of olivine-phyric Shergottite Y980459: petrogenesis of depleted Shergottites. Antarct. Meteor. Res. 18, 46–65.

Shirai, N., Ebihara, M., 2004. Chemical characteristics of a Martian meteorite, Yamato 980459. Antarct. Meteor. Res. 17, 55.

Spandler, C., O'Neill, H.S.C., 2010. Diffusion and partition coefficients of minor and trace elements in San Carlos olivine at 1300 °C with some geochemical implications. Contrib. Mineral. Petrol. 159, 791–818. http://dx.doi.org/10.1007/s00410-009-0456-8.

Symes, S.J.K., Borg, L.E., Shearer, C.K., Irving, A.J., 2008. The age of the martian meteorite Northwest Africa 1195 and the differentiation history of the shergottites. Geochim. Cosmochim. Acta 72, 1696–1710. http://dx.doi.org/10.1016/j.gca.2007.12.022.

Tuff, J., Gibson, S.A., 2007. Trace-element partitioning between garnet, clinopyroxene and Fe-rich picritic melts at 3 to 7 GPa. Contrib. Mineral. Petrol. 153, 369–387. http://dx.doi.org/10.1007/s00410-006-0152-x.

Tuff, J., Wade, J., Wood, B.J., 2013. Volcanism on Mars controlled by early oxidation of the upper mantle. Nature 498, 342–345. http://dx.doi.org/10.1038/nature12225.

Usui, T., McSween Jr., H.Y., Floss, C., 2008. Petrogenesis of olivine-phyric shergottite Yamato 980459, revisited. Geochim. Cosmochim. Acta 72, 1711–1730. http://dx.doi.org/10.1016/j.gca.2008.01.011.

Usui, T., Sanborn, M., Wadhwa, M., McSween, H.Y., 2010. Petrology and trace element geochemistry of Robert Massif 04261 and 04262 meteorites, the first examples of geochemically enriched lherzolitic shergottites. Geochim. Cosmochim. Acta 74, 7283–7306. http://dx.doi.org/10.1016/j.gca.2010.09.010.

Usui, T., Alexander, C.M.O.D., Wang, J., Simon, J.I., Jones, J.H., 2012. Origin of water and mantle–crust interactions on Mars inferred from hydrogen isotopes and volatile element abundances of olivine-hosted melt inclusions of primitive shergottites. Earth Planet. Sci. Lett. 357, 119–129. http://dx.doi.org/10.1016/j.epsl.2012.09.008.

Wadhwa, M., McSween Jr., H.Y., Crozaz, G., 1994. Petrogenesis of shergottite meteorites inferred from minor and trace element microdistributions. Geochim. Cosmochim. Acta 58, 4213–4229. http://dx.doi.org/10.1016/0016-7037(94)90274-7.

Welsch, B., Faure, F., Famin, V., Baronnet, A., Bachèlery, P., 2013. Dendritic crystallization: a single process for all the textures of olivine in basalts? J. Petrol 54 (3), 539–574. http://dx.doi.org/10.1093/petrology/egs077.